Development of a UAV-based fully-airborne transient electromagnetic system

Feng Guo[1], Ling Huang[1], Jiankai Li[1], Guangyou Fang[1,2], Lihua Liu[1], Xiaojun Liu[1],

[1]Aerospace Information Research Institute, Chinese Academy of Sciences, Beijing 100045, China
[2] Greater Bay Area Branch of the Aerospace Information Research Institute, Guangzhou 510530, China

Correspondence to: Ling Huang (huangling@aircas.ac.cn)

Abstract. In response to the challenges of transient electromagnetic (TEM) exploration in complex terrain, a lightweight, low-noise, three-component, fully-airborne TEM system based on an unmanned aerial vehicle (UAV) platform is designed, offering improved terrain adaptability and survey efficiency compared with existing semi-airborne UAV-based TEM systems. Three-component electromagnetic field measurement enables reliable detection of the normal component, even over undulating terrain, and provides a theoretical basis for correcting errors caused by receiver coil oscillation. Through system-level optimization, the proposed system achieves a balance between weight and transmission power, featuring a lightweight configuration(14.94 kg), a large transmitting magnetic moment (2250 Am²), and an extremely low system dynamic noise level (1.7 nT/s). A series of performance verification experiments and field tests verify the stability and practical operability of the proposed system under field application. Furthermore, comparisons between the inversion results obtained from the acquired survey data and borehole logging data provide additional evidence of the system's reliability. Therefore, this system offers an effective technical approach and solid data support for the fine detection of subsurface interfaces at depths of up to 50 m.

1 Introduction

In recent years, TEM methods have become indispensable in geophysical studies including but not limited to mineral exploration (Steuer et al., 2020), hydrogeological mapping (Podgorski et al., 2013), freshwater investigation (Siemon et al., 2011) due to the high sensitivity to conductive targets. The airborne electromagnetic Method (AEM) was proposed in the early middle of 20th century to further improve survey efficiency (Wu et al., 2019). Over the past few decades, fixed-wing aircraft and helicopter have become the mainstream platform owing to their heavy-lift capability. Helicopter-based platform, in particular, outperformed due to its low-altitude flight performance. The VTEM series is a premier helicopter-borne TEM system that adopts a high-power concentric-loop configuration. Based on different dipole moment and loop diameter, this series consists of VTEM Plus, VTEM Max and VTEM ET (Laizer et al., 2025). The SkyTEM system is one of the most sophisticated helicopter-borne transient electromagnetic (HTEM) platform as well. This series features a rigid, dual-moment transmitter configuration, which enables simultaneous mapping of high-resolution near-surface resistivity and deep geological conductors (Auken et al., 2009).

Although traditional helicopter-borne systems offer extensive coverage, their high operational costs and logistical constraints in rugged terrain often limit their applicability. The emergence of UAVs has revolutionized this field by providing a lower-

Deleted: order

Deleted:

Formatted: Font: (Default) Times New Roman, (Asian) Times New Roman

Deleted: Transient Electromagnetic (

Deleted: s

altitude, terrain-following alternative. As a carrier platform of various types of sensors, UAV have already become increasingly popular in other geophysical surveys including magnetic exploration (Kolster et al., 2022), ground-penetrating radar (López et al., 2022), LiDAR (Noviello et al., 2021) as well as integrated approaches such as combined photogrammetry and magnetometry (Martelet et al., 2021). In contrast, most of current UAV-based TEM implementations rely on semi-airborne configuration utilizing a ground stationary transmitter and a drone-towed receiver, which restricts mobility in inaccessible regions (Dadrass Javan et al., 2024).

Therefore, efforts toward developing a true fully-airborne drone TEM system, where both the transmitter and receiver are integrated into the flight platform, have continued unabated. A UAV-based TEM system named SkyTEM21HR has been successfully conducted for geotechnical ground investigation, whose data is proved to be useful, and the spatial sampling rate has been improved due to the drone platform. Nevertheless, the system still weighs 150kg, requiring a heavy-lift drone for field operations (Nyboe et al., 2024). Tang et al. (2026) developed Wukong system for goaf detection with 80000 Am^2 transmitting magnetic moment but measures only one component. This system has been proved to be effective as its strong ability to identify anomalies. Apart from a unified transmission and receiver platform integrated on one drone, a dual drone configuration named NEXT system developed by Radai Ltd. revealed another option. In that case, the compact mobile transmission loop is carried by a drone while the response is detected with a receiver transported by another drone (Pirttijärvi et al., 2022). Despite its potential, such a fully-airborne system faces substantial challenges, including strict UAV payload limits, the electromagnetic interference (EMI) generated by drone motors and the requirement for lightweight yet high-power transmission. These constraints necessitate various engineering compromises in the systems outlined above.

However, previous studies have demonstrated that various approaches have been developed for near-surface airborne geophysical exploration, yet each with distinct advantages and limitations. Eppelbaum and Mishne (2011) proposed the UAV-borne magnetic and VLF-EM measurements, providing a high mobility and ground-following flight capability for geophysical exploration over mountainous and complex terrain. The proposed method, however, utilized an active time-domain electromagnetic technique, can reconstruct vertical electrical structures and detect conductive targets such as water-bearing fractures even for non-magnetic subsurface media. For manned airborne electromagnetic surveys, Siemon (2012) developed precise 1-D forward and inverse algorithms for helicopter-borne high-frequency EM data, which mainly resolve shallow subsurface structures and rely on costly manned helicopter platforms with limited accessibility in rugged terrain.

This paper presents a novel fully-airborne TEM system designed to address these challenges through developing a lightweight 3-component magnetic sensor to realize real terrain-following exploration problem by obtain vertical normal component of uneven terrain. Meanwhile, to enhance the operational capabilities in steep mountainous terrain, a lightweight structural design is implemented.

Deleted: e.g.
Deleted: -
Formatted: English (US)
Deleted: the pursuit of achieving
Deleted: has never ceased
Deleted: n
Deleted: was
Deleted: However
Deleted: therefore a heavy-lift drone is necessary for filed operation…
Deleted: yet only 1 component
Deleted: ,
Deleted: and the
Deleted: icient
Deleted: significant
Deleted: the
Deleted: of UAVs
Deleted: need
Deleted: That's the reason for various compromises existing in the aforementioned systems.
Formatted: Font: (Default) SimSun, (Asian) SimSun, English (US)

2 System design and development

The system is designed to weigh less than 15 kg, allowing it to be easily transported by light-lift UAVs (e.g., DJI T60 and DJI FC30). This enables deployment by smaller work teams in complex terrain. Various optimizations, ranging from equipment development to structural design, have been implemented to achieve these objectives, as illustrated in Fig. 1.

In this system, electromagnetic compatibility among the individual components is carefully considered at the design stage. Accordingly, a separated configuration is adopted for the electronic devices and the towed bird. The TEM transceiver consists of a transmitter, a receiver and high-density lithium battery for power supply. Through the formed binding cable and the attached electrical cable, the transceiver is connected to the towed bird to ensure the simplicity and stability of the overall structure.

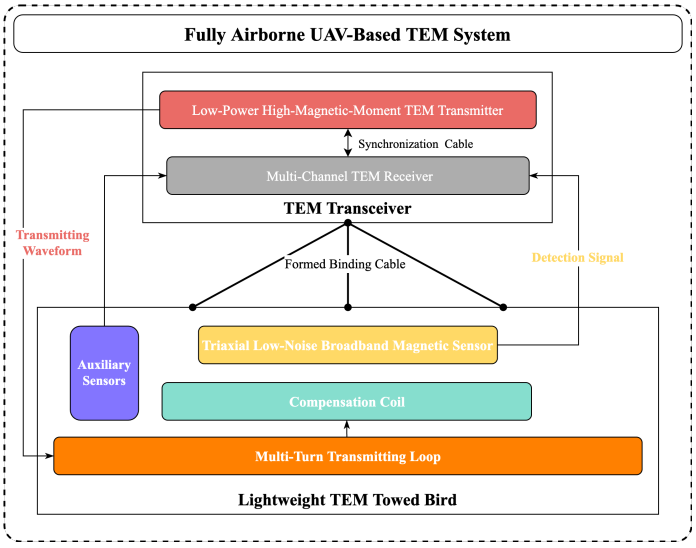

Figure 1 System structural design

2.1 Design and development of low-power high-magnetic-moment TEM transmitter

This research on high-frequency pulse fast turn-off technology was conducted to achieve TEM transmission with rapid current turn-off, high transmitter magnetic moment, low power consumption, and compact form factor. The dual-clamping topology applies high-voltage clamping to both the positive and negative edges of the transmit current, enabling linear, fast edge ramps and supporting the generation and precise regulation of high-quality electromagnetic pulse waveforms. As shown in Fig. 2,

Deleted: The system is designed to be lighter than 15kg for an easily equipment with a lighter-lift UAV (e.g. DJI T60, DJI FC30). In that case, smaller work group is capable for deployment on complex terrain. Optimizations from equipment development to structural design are conducted to achieve the above-mentioned aims as the Fig.1 illustrated.¶

Deleted: during each part

Deleted: well

Deleted: therefore a separated structure

Deleted: of the electronic devices and the towed bird is applied.

Deleted:

Deleted: and

Deleted: as well as their

Formatted: Font: (Default) Times New Roman, (Asian) Times New Roman

Deleted: pod

Deleted: e

Deleted: shutdown

Deleted: shutdown

Deleted: large

Deleted: size

Deleted: Based on constant-voltage dual-clamp transmission technology, the power circuit of the transmission system employs segmented optimizations techniques in the transmission current waveform. Dual clamping can simultaneously clamp the rising and falling edges of the current with high voltage, achieving a rapid and linear rise or fall of the edges, enabling the generation and high-precision control of high-quality electromagnetic pulse signals.

through a segmented control design that divides the positive edge into a clamping stage and an exponential stage, the electromagnetic response excited by the positive edge of the high-frequency pulse does not interfere with that induced by the negative-edge turn-off excitation. The power switching and power inverter circuits transmit dual pulses, with both large and small magnetic moments to achieve blind zone suppression and high-precision detection in both deep and shallow areas. While increasing the peak transmission current, the TEM pulse width is further compressed to reduce the power consumption.

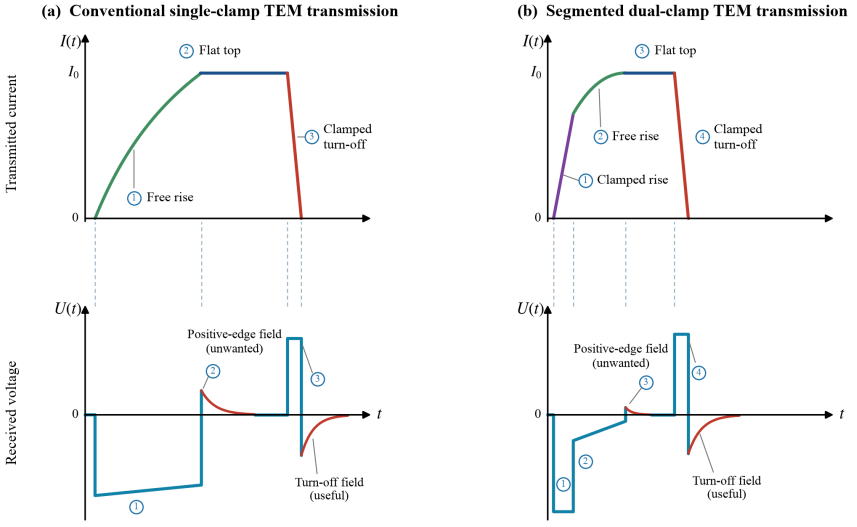

Figure 2 Timing diagram for segmented dual-clamping transmitters

The proposed TEM transmitter adopts a high-speed power switching architecture for power inversion, rapid supply commutation, and segmented adjustable active constant-voltage dual clamping. Three galvanically isolated internal power supplies are deployed to mitigate electrical crosstalk and improve control stability. The power components adopted a high-speed MOSFET full-bridge inverter circuit to achieve rapid shut-down and improve detection resolution.

Transmitter function and performance tests, as well as synchronous transmit/receive decoding tests were conducted. And Fig. 3 illustrates the test results of the actual transmitted pulse, verifying that the system can generate alternating high- and low-current dual pulses. The transmit current exhibits excellent stability within the flat-top interval and across successive pulse cycles. Under 24V power supply conditions, the dual-clamping constant voltage up to 500V could be reached, and the clamping voltage level remains stable during current shutdown, ensuring the linearity of shutdown current. Transmission capability experiments with an equivalent load proved that the transmitted current could reach 20A±0.3A, with a turn-off time of 12μs@20A.

Deleted:

Deleted: transient electromagnetic

Formatted: Caption

Deleted: A high-speed power switch design was conducted on the proposed TEM transmitter to achieve power inversion, rapid power supply switching, as well as dual clamping of active constant voltage which is segmented adjustable.

Deleted: It utilized three sets of isolated power supplies internally to eliminate crosstalk and enhance system control stability

Deleted: 2

Deleted: which demonstrated that the TEM transmitter achieved alternating large and small current dual-pulse transmission,

Deleted: and that the transmitted current exhibited high stability both during the flat-top period and between repetitive periodic pulses.

Deleted: up to

Formatted: Font: (Default) Times New Roman Regular, (Asian) Times New Roman

Formatted: English (US)

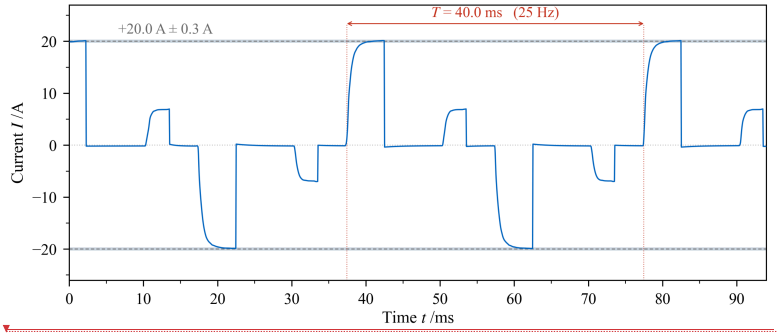

Figure 3 Test result of transmitted pulse current

2.2 Development of multi-channel signal acquisition technology

The multi-channel signal receiver mainly completes the signal acquisition and recording from the triaxial electromagnetic field sensor, including signal conditioning, analog-to-digital conversion, data storage, and data quality monitoring. The internal structure design is illustrated in Fig. 4, where OCXO denotes an oven-controlled crystal oscillator, PL the programmable logic, and PS the processing system. The latter two being the two sections of the Zynq system-on-chip.

The triaxial electromagnetic field signal is processed by a protection circuit and impedance matching before being input to a low-noise differential amplifier circuit, where DC bias compensation is implemented. To meet the requirements of signal acquisition in large dynamic range, the subsequent stage is designed based on a programmable gain amplifier circuit with 1/4, 1, 4, 8, and 16 times gain adjustment to regulate the signal amplitude. Finally, after anti-aliasing filtering, the signal is input to an analog-to-digital converter (ADC) circuit for acquisition.

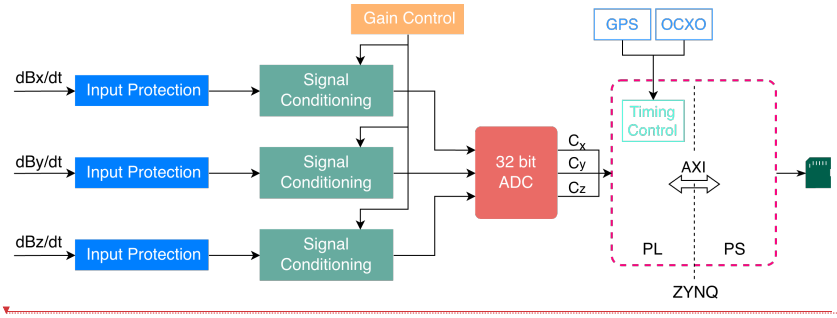

Figure 4 Block diagram of developed signal receiver

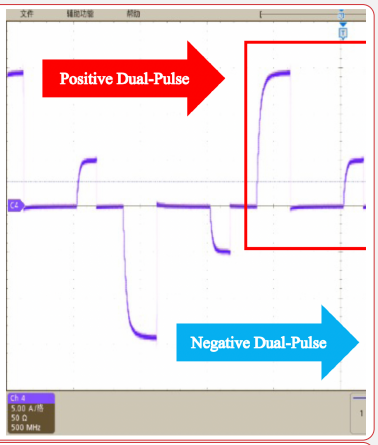

Deleted:
Deleted: 2
Deleted: Research
Deleted: on
Deleted: magnetic
Deleted: The circuit design and internal structure is illustrated in Fig. 3.
Deleted: magnetic

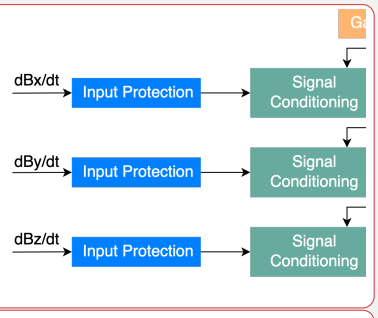

Deleted:
Deleted: 3
Formatted: Font: (Default) SimSun, (Asian) SimSun, (Asian) Chinese (China), (Other) English (US)

The system adopts the LTC2500 true 32-bit ADC to realize high-precision and high-speed signal acquisition with a maximum sampling rate of 1Msps. High-speed sampling is performed at the front end, followed by SSINC digital filtering to achieve low-sampling-rate data output, which significantly improved the dynamic range to approximately 138dB@1 Ksps (FS=±5Vpp). The central controller of the receiving system is selected as ZYNQ7020. The PL end, which acts as the FPGA, handles the acquisition of the ADC-digitized data and FIR data filtering, sending it to the ARM processor at the PS end via the AXI bus. The ARM processor then caches the data in double data rate (DDR) memory.

The receiver also integrates a high-precision synchronous clock calibration circuit to provide the system with highly stabled local synchronous clock signal for time matching between the transmitter and receiver. Alternatively, time synchronization can be achieved via a synchronization cable connection.

Finally, the evaluation test was conducted after integration, and the dynamic noise level of the system will be discussed in the following section.

2.3 Design of triaxial low-noise broadband electromagnetic sensor

Through optimization methods study for the distributed impedance parameters of the sensor coil and impedance matching techniques, the bandwidth optimization design of the sensor coils was achieved. Capacitor compensation technology was employed, and a capacitor compensation network at the front end of the low-noise amplifier circuit was introduced to reduce the coil capacitance and increase the resonant frequency effectively. An optimized design of a hollow coil electromagnetic field sensor based on a ribbon cable structure was implemented. By setting the coils in the optimal damping state, effective acquisition of early-time high-frequency secondary field signals as well as weak late-time secondary field signals was enabled. The triaxial electromagnetic sensor was designed in a hemispherical structure shown in the Fig. 6(a). Apart from receiving coils, a low-noise signal amplification was also integrated using a bipolar transistor and a low-noise instrumentation amplifier, while impedance matching was also implemented.

The designed sensor directly measures the time derivative of the magnetic field dB/dt, rather than the magnetic field B. The HNOM (nominal magnetic field transfer coefficient) shown in Fig. 5(b) characterizes this transfer relationship, whose magnitude increases linearly with frequency and presents an inherent high-pass response. As Tumański (2007) summarized, the differentiating coil has no flat passband to serve as a reference gain level, so the -3 dB bandwidth criterion is not adopted in this work (Metwally, 2013). The sensitivity of the sensor was tested, and the measured frequency response results are shown in the Fig. 5(b). The receiving bandwidth of the electromagnetic field sensor is wider than 120kHz.

Deleted: e

Deleted: ¶

Formatted: Not Highlight

Formatted: Not Highlight

Formatted: Not Highlight

Formatted: Not Highlight

Deleted: The noise level of receiver was tested, and the results are shown in Fig.4, from which the dynamic noise level of the signal receiver at the 1ms sampling window are shown as 0.145 μV (Z), 0.147 μV (X), and 0.16 μV (Y).

Formatted: Highlight

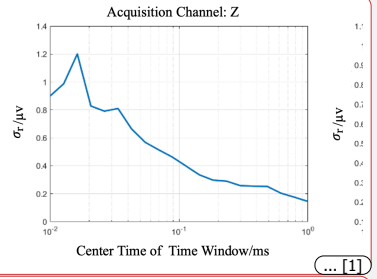

Deleted: ... [1]

Deleted: 5

Deleted: 5

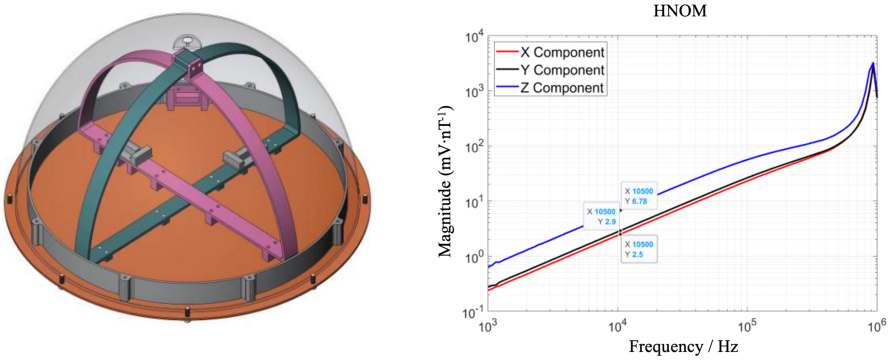

Figure 5 Developed electromagnetic field sensor. (a) Designed structure; (b) Measured frequency response

Deleted: 5

2.4 Design of lightweight TEM towed bird

The fully-airborne TEM detection towed bird, illustrated in Fig. 6, carries the transmitting coil, compensation coil, and triaxial electromagnetic sensor, making it a unified transceiver detection device with common-center transmission and reception, stable primary field compensation, and orthogonal three-component sensors. The towed bird adopted a regular dodecagon structure, on which the transmitting loop is carried. The equation for calculating the transmitting magnetic moment is as follows:

Deleted: 6

$$M = N * I * n \frac{r^2}{2} sin(\frac{2\pi}{n}), \quad (1)$$

Deleted: ¶

Formatted: Left, Indent: First line: 2 ch

Where n is the number of sides of the polygon, here n=12; r is the radius of the circumscribed circle, which is 2.5 m; N is the number of turns of the transmitting coil; and I is the peak transmitting current. The transmitting module is designed with a peak transmitting current of 10 A-20 A and 6 turns, therefore the transmitting magnetic moment is calculated as 1125 Am² - 2250 Am².

Deleted: N

Formatted: Font: Italic

Deleted:

Deleted:

The transmitting coil adopts a primary-field compensation technique at the centre to suppress the electromagnetic response of conventional TEM systems arising from the turn-off time and the mutual inductance effect between the transmitting and receiving coils. This approach compensates the strong primary field component in the received signals, achieves weak coupling between the transmitting and receiving coils.

Deleted: ¶

To achieve lightweight design of towed-bird, carbon fibre material is used to form the transmitting loop supporting former. A novel scheme with integrated loop structure is devised to lower the aerodynamic drag and mass of the transmitting coil.

Formatted: Font: (Default) SimSun, (Asian) SimSun

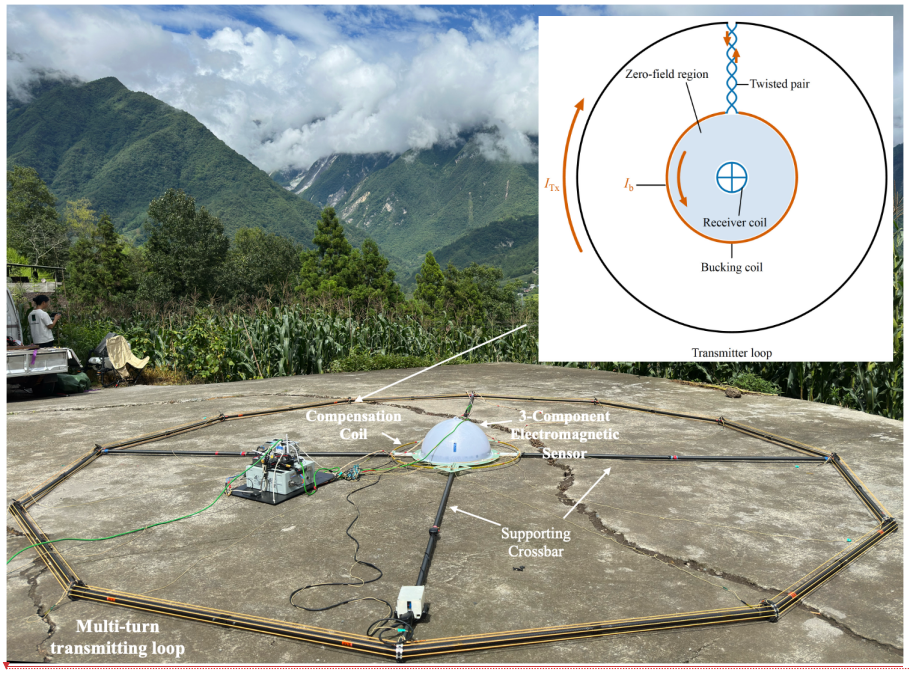

Figure 6 Design of lightweight TEM towed-bird

Deleted:



Deleted: 6

3 System integration and evaluation

To achieve a fully airborne TEM system, the integration method also has a significant impact on the final performance. The proposed device employed a non-electrical connection design with the UAV, which improved the compatibility with the flight platform. This design also enhanced the system's electromagnetic compatibility, resulting in a better signal-to-noise ratio. Simultaneously, the auxiliary radar altimeter and Inertial Measurement Unit (IMU) were mounted on the supporting crossbar to acquire the position and altitude of the towed bird, facilitating correction and analysis during data processing. From Fig. 7, the system integration result is given.

Deleted: 7

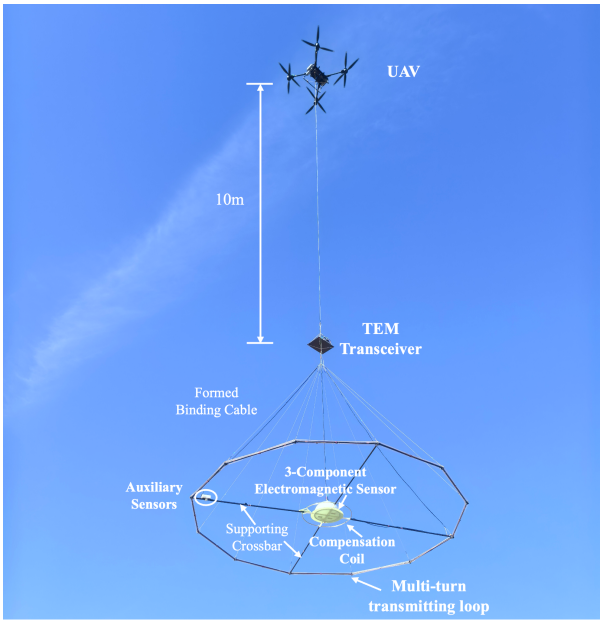

Figure 7 System integration

Deleted: 7

After system integration, evaluation tests and experiments were conducted on various performance indicators of the system, and the key technical indicators are listed as Tab. 1. Compared with current state-of-art UAV fully-airborne TEM systems (Wang et al., 2021; Nicklas et al., 2023), the UAV-HTEM-5M proposed in this paper achieved a better balance between system weight and transmitting magnetic moment, while the other indicators are also at an advanced level. It is worth noting that this system has significant advantages in receiving all electromagnetic field components (three components) and noise level indicators, and its practical application results will be discussed in following section.

Table 1 Comparison of state-of-art systems with proposed system

Affiliation	SkyTEM Surveys	Chongqing Uni.	Jilin Uni.	Aerospace CAS
System	SkyTEM21HR	Wukong DTEM70	TEM-31	**UAV-HTEM-5M**
Sensor Component	1C	1C	1C	**3C**
Towed-Bird Dimension	——	Ø1.5, 4, 5, 7, 8, 10 m	2 m×2 m	Ø 5 m
Transmitting Moment	3480 Am^2	34000 Am^2	360 Am^2	2250 Am^2

Formatted Table

Deleted: 100-1

Deleted: 12

Deleted: 80000

Acquisition Bandwidth	900 kHz	——	≈ 60 kHz	120 kHz
Noise Level	——	——	≈ 10 nT/s	**1.7 nT/s**
System Weight	150 kg	40 kg	8 kg	14.94 kg

3.1 Analysis of system dynamic noise

The dynamic noise of an integrated airborne system is the noise level that the complete instrument reaches when it is carried by the aircraft and records data in flight. It therefore includes contributions that a bench test cannot reproduce, so the noise level is estimated from the scatter of the gate amplitudes between successive soundings rather than from the electronic noise of the receiver alone (Macnae et al., 1984):

Airborne TEM system uses the following expression to evaluate the dynamic noise level of the sounding system:

$$N_{d,j} = \sqrt{\frac{1}{N-1}\sum_{i=1}^{N}\left(d_{ij} - \bar{d}_j\right)^2}, \quad (2)$$

where d_{ij} is the amplitude of gate j in the ith sounding, $\bar{d}_j$ its mean over the N soundings, and $N_{d,j}$ the noise of the gate, in nT/s.

The maximum designed sounding depth of the integrated UAV-borne system is 50 m. From the resistivity of a typical geological body, the latest TEM signal time that the system has to observe can be calculated as follows (Nabighian, 1979; Nabighian and Macnae, 1991):

$$\delta_{\mathrm{TD}} = \sqrt{\frac{2\rho t}{\mu_r \mu_0}}, \quad (3)$$

where δ_{TD} is the maximum sounding depth of the system, in m; t is the TEM propagation time, in s; ρ is the resistivity of the typical geological body, in Ω·m; μ_r is the relative permeability of the medium, dimensionless; and μ_0 is the permeability of free space, $4\pi\times10^{-7}$ H/m.

The test was carried out with the transmitter off and the towed bird flying at survey speed (2-4 m/s) more than 50 m above ground, continuous data were recorded at a sampling rate of 256 kHz and then decimated into time gates following standard TEM data processing procedures. Using the effective area of the sensor, the noise voltage at the receiver is converted to equivalent input magnetic field noise. The dynamic noise level of the late-time gate at 1 ms is calculated and compared with the acceptance threshold of 2 nT/s, a value below which indicates that the system has enough signal-to-noise ratio for the design exploration depth.

Figure 8 shows the equivalent input magnetic-field noise of the three receiving channels on logarithmic axes. At the 1 ms gate the equivalent input noise is 1.30 nT/s in Z, 1.70 nT/s in X and 0.82 nT/s in Y respectively. The integrated system therefore meets the design target of less than 2 nT/s in all three channels.

Deleted: ——
Formatted: Font: 10 pt, (Asian) Chinese (China), (Other) English (US)
Formatted: Indent: First line: 0 cm
Formatted ... [2]
Formatted ... [3]
Formatted ... [4]
Formatted: (Asian) Chinese (China), (Other) English (US)
Formatted ... [5]
Formatted: (Asian) Chinese (China), (Other) English (US)
Formatted ... [6]
Formatted: Indent: First line: 0 cm
Formatted ... [7]
Formatted ... [8]
Formatted ... [9]
Formatted ... [10]
Formatted ... [11]
Formatted ... [12]
Formatted ... [13]
Formatted ... [14]
Formatted ... [15]
Formatted ... [16]
Formatted: (Asian) Chinese (China), (Other) English (US)
Formatted ... [17]
Formatted ... [18]
Formatted: Indent: First line: 0 cm
Formatted ... [19]
Formatted ... [20]
Formatted ... [21]
Formatted ... [22]
Formatted: (Asian) Chinese (China), (Other) English (US)
Formatted ... [23]
Formatted ... [24]
Formatted ... [25]
Formatted ... [26]
Formatted ... [27]
Formatted ... [28]
Formatted ... [29]
Formatted: (Asian) Chinese (China), (Other) English (US)

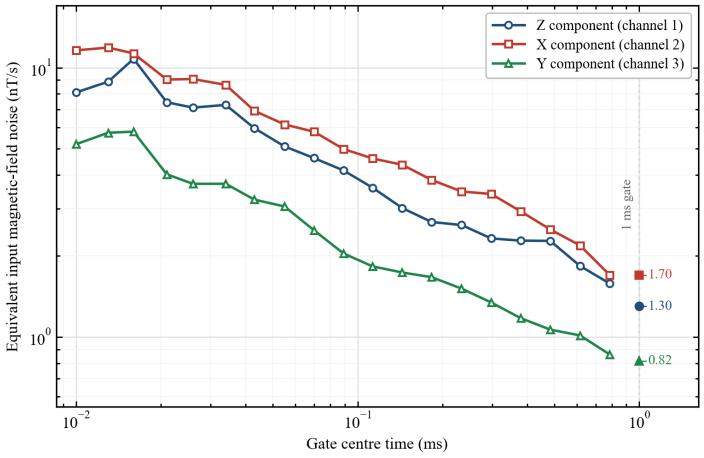

Figure 8 Equivalent input magnetic-field noise of the three receiver channels

3.2 Design of electromagnetic compatibility

Generally, there are two independent noise sources originated from the UAV platform: electromagnetic interference (EMI) radiated by the rotor motors and their drive electronics which coupled into the receiving coil through the near field, and motion noise arising from the swinging and rotation of the towed bird. A larger separation of suspension length attenuates the near-field magnetic coupling, which for a dipole-like source falls off as, whereas an excessive length degrades the stability of the towed bird and elevates the low-frequency motion noise. The suspension length was therefore treated as a trade-off parameter to be fixed experimentally rather than simply maximized.

Comparative trials were carried out at site with low background noise, with the cable length set to 6, 10 and 12 m separately. The transmitter was switched off, and the coil was kept more than 50 m above ground throughout. With increasing suspension length, the narrow-band interference in the 70–95 kHz bands decreased markedly, and the spectrum above 1 kHz became smoother, indicating that a longer suspension suppresses the coupling of motor EMI into the coil. At 12 m, however, the bird oscillated visibly and pronounced baseline drift and low-frequency motion noise appeared in the raw data, degrading data quality.

However, noises originated from different UAV platforms differs in both frequency band and amplitude, and the proposed system is not designed for a particular flight platform. Therefore, in addition to electromagnetic compatibility, the safe distance for terrain-following flight and the safe operating clearance during take-off and landing are also important considerations, as some UAV platforms are restricted to a limited ground clearance by regulations.

Formatted: Justified
Formatted: Not Highlight
Formatted: Caption, Space After: 0 pt, Line spacing: single
Formatted: (Asian) Chinese (China), (Other) English (US)
Formatted: Font: (Default) Times New Roman, 10 pt, (Asian) Chinese (China), (Other) English (US)
Formatted: Font: (Default) Times New Roman, 10 pt, (Asian) Chinese (China), (Other) English (US)
Formatted: Normal, Space After: 0 pt, Pattern: Clear
Formatted: Font: (Default) Times New Roman, 10 pt, (Asian) Chinese (China), (Other) English (US)
Formatted: Font: (Default) Times New Roman, 10 pt, (Asian) Chinese (China), (Other) English (US)
Formatted: Font: (Default) Times New Roman, 10 pt, (Asian) Chinese (China), (Other) English (US)
Formatted: Font: (Default) Times New Roman, 10 pt, (Asian) Chinese (China), (Other) English (US)
Formatted: Font: (Default) Times New Roman, 10 pt
Formatted: Font: (Default) Times New Roman, 10 pt, (Asian) Chinese (China), (Other) English (US)
Formatted: Font: (Default) Times New Roman, 10 pt, (Asian) Chinese (China), (Other) English (US)
Formatted: Font: (Default) Times New Roman, 10 pt, (Asian) Chinese (China), (Other) English (US)
Formatted: Font: (Default) Times New Roman, 10 pt, (Asian) Chinese (China), (Other) English (US)
Formatted: Font: (Default) Times New Roman, 10 pt, (Asian) Chinese (China), (Other) English (US)

3.3 Analysis of detection depth

A two-layer geoelectric model was built to represent the typical electrical structure of a non-explicit landslide hazard. The resistivity of the upper layer was set to 20 Ω·m and that of the lower layer to 800 Ω·m. The depth of the interface between the two media was varied from 5 m to 50 m; for each interface depth, the responses of two models differing in interface depth by 1 m were computed and subtracted, so that the residual represents the signal produced by a 1 m offset of the interface.

The proposed system was assumed to fly at 5 m above the ground surface with a transmitting magnetic moment of 2250 A·m², which corresponds to the configuration of the proposed system.

The latest usable time gate that could be simulated is controlled mainly by the resistivity of the upper layer. In a homogeneous half-space, the transient field diffuses downwards as a smoke ring whose depth grows as $\sqrt{\rho t/\mu_0}$ (Nabighian, 1979; Raiche and Gallagher, 1985), and a buried interface becomes resolvable once the diffusion front has passed it, that is, at about one diffusion depth of overburden (Spies, 1989; Christiansen and Auken, 2012). The latest usable time gate is therefore estimated from

$$t = \frac{H^2}{784\rho}, \tag{4}$$

where t is the delay after turn-off (ms), H is the maximum detection depth (m) and ρ is the apparent resistivity (Ω·m). Equation (4) is not the analytical smoke-ring solution, but a practical engineering approximation for estimating the latest interpretable late-time gate. In this study, it is used only to select the evaluation time gate for noise assessment, rather than for rigorous depth of investigation inversion. For a two-layer medium the target is the interface itself, so the background apparent resistivity reduces to the resistivity of the upper layer.

For an upper-layer resistivity of 10 Ω·m, equation (4) gives the latest simulation time of 0.3 ms. The analysis of slip surfaces and groundwater levels shallower than 50 m is therefore restricted to delays shorter than 0.3 ms. Within this window the response difference produced by a 1 m offset of the interface was compared with the dynamic noise level of the system, a difference being regarded as detectable only when it exceeds that level.

The maximum difference was extracted along the depth axis between 10 m and 80 m, and the response differences against interface depth are illustrated in Fig. 9. The grey dashed horizontal line marks the dynamic noise level of the system, taken conservatively as 2 nT/s.

Between 5 and 50 m the difference produced by a 1 m offset of the interface remains above 2 nT/s, therefore exceeds the dynamic noise level of the developed system at every interface depth considered. A response difference induced by 1 m displacement of the slip surface is thus theoretically observable by the proposed system within the 50 m depth range of interest.

Formatted: English (US)

Formatted: Font: 10 pt, (Asian) Chinese (China), (Other) English (US)

Formatted: Indent: First line: 0 cm, Line spacing: 1.5 lines

Formatted: Font: 10 pt, (Asian) Chinese (China), (Other) English (US)

Formatted: Font: 10 pt, (Asian) Chinese (China), (Other) English (US)

Formatted: Font: 10 pt, (Asian) Chinese (China), (Other) English (US)

Formatted: Font: 10 pt, (Asian) Chinese (China), (Other) English (US)

Formatted: Indent: First line: 2 ch, Space Before: 0 pt, After: 0 pt, Line spacing: 1.5 lines, Tab stops: Not at 7.32 cm + 14.65 cm

Formatted: Font: 10 pt, (Asian) Chinese (China), (Other) English (US)

Formatted: Font: 10 pt, (Asian) Chinese (China), (Other) English (US)

Formatted: Font: 10 pt, (Asian) Chinese (China), (Other) English (US)

Formatted: Font: 10 pt, (Asian) Chinese (China), (Other) English (US)

Formatted: Font: 10 pt, (Asian) Chinese (China), (Other) English (US)

Formatted: Font: 10 pt, (Asian) Chinese (China), (Other) English (US)

Formatted: Indent: First line: 0 cm, Line spacing: 1.5 lines

Formatted: Font: 10 pt, (Asian) Chinese (China), (Other) English (US)

Formatted: Font: 10 pt, (Asian) Chinese (China), (Other) English (US)

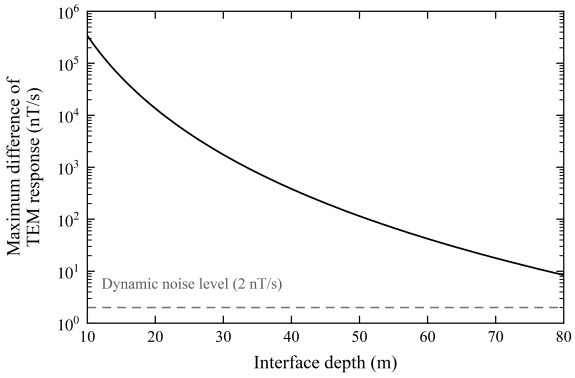

Figure 9 Airborne TEM response difference versus depth

4 Calibration of the vertical component based on 3-component electromagnetic field data

In current TEM studies and applications, usually only the vertical component of electromagnetic field is recorded rather than all three components, which mainly attributes to the complexity of instrument system and the difficulty of data processing. However, former studies have proved that all-component interpretation takes more advantages in determining the range of anomalies and improving vertical and horizontal resolution (Chen et al., 2008). Yu et al. (2021) demonstrated that the 3-component TEM measurement has the potential of giving access to conductor information and the extension direction of anomalous body by numerical simulation.

For a better support of 3-component TEM data processing, a simultaneous 3-component TEM sensing and acquisition technology was studied and developed in this paper. The increase of system complexity, however, brought higher noise level, which should be considered from the system design.

To better eliminate measurement errors caused by changes in sensor attitude, IMU (Inertial Measurement Unit) information was introduced, and a more complete attitude correction model can be constructed, providing data foundation for accurate inversion and modeling of complex underground geological bodies.

The coordinate of IMU (coil attitude) and the standard geographical system could be transformed using a rotation matrix. Under this circumstance, a cartesian coordinate system with the x-axis pointing east, the y-axis pointing north, and the z-axis pointing upwards was established. Define $\phi(t)$, $\theta(t)$, and $\psi(t)$ as the time-varying roll angle, pitch angle, and yaw angle, respectively. On this basis, the rotation matrix is formulated as follows:

Formatted: Normal

Deleted: 9

Deleted: ASD of electromagnetic interference caused by UAV (DJI T100)....

Deleted: using

$$R = R_\psi R_\theta R_\varphi = \begin{bmatrix} cos\,\psi & -sin\,\psi & 0 \\ sin\,\psi & cos\,\psi & 0 \\ 0 & 0 & 1 \end{bmatrix} \begin{bmatrix} cos\,\theta & 0 & sin\,\theta \\ 0 & 1 & 0 \\ -sin\,\theta & 0 & cos\,\theta \end{bmatrix} \begin{bmatrix} 1 & 0 & 0 \\ 0 & cos\,\varphi & -sin\,\varphi \\ 0 & sin\,\varphi & cos\,\varphi \end{bmatrix}, \quad (5)$$

Based on the rotation matrix, the normal vector of the coil could be expressed as follows:

$$\boldsymbol{n}_{coil} = R_{13}(t)\vec{\imath} + R_{23}(t)\vec{\jmath} + R_{33}(t)\vec{k}, \quad (6)$$

where $\boldsymbol{n}_{coil}$ denotes the instantaneous normal vector of the coil in the geographic (ENU) coordinate system. $R_{13}(t)$, $R_{23}(t)$, $R_{33}(t)$ are the elements in the of the time-varying rotation matrix $\boldsymbol{R}(t)$. $\vec{\imath}$, $\vec{\jmath}$, $\vec{k}$ are the unit vectors along the east, north and upward axes of the ENU geographic coordinate system, respectively.

A transformation relationship between IMU coordinate (B') and geographic coordinate (B) was established as follows:

$$B = R \cdot B', \quad (7)$$

Therefore, we have:

$$\begin{aligned} B_x &= R_{11}B'_x + R_{12}B'_y + R_{13}B'_z, \\ B_y &= R_{21}B'_x + R_{22}B'_y + R_{23}B'_z, \quad (8) \\ \boldsymbol{B_z} &= \boldsymbol{R_{31}B'_x + R_{32}B'_y + R_{33}B'_z}, \end{aligned}$$

For each acquisition point, the rotation matrix could be expressed by real time measurement of IMU, and the calibrated response could be calculated using the aforementioned equations (5-8) and the pre-known system HNOM.

The vertical component calibration of the electromagnetic response effectively suppresses interference caused by attitude variations and surface or near-surface inhomogeneities, yielding a more accurate reflection of deep-seated targets. To quantitatively evaluate the effectiveness of the attitude compensation algorithm, Pearson correlation coefficients between the coil response and inertial navigation attitude data were calculated before and after correction. The overall correlation coefficients corresponding to the x- and y-axis components decrease markedly. Meanwhile, the correlation between coil outputs and roll/pitch angles becomes insignificant, which demonstrates that the attitude-dependent interference is effectively suppressed. Improvements are also observed in the vertical-component electromagnetic responses, where the average relative correlation coefficient decreases by 10.9% with respect to pitch angle and 26.8% with respect to roll angle.

The attitude-corrected three-component electromagnetic responses are illustrated in Fig. 10. Motion noise caused by attitude variations in the x- and y-axis components has been substantially suppressed. In contrast, the intrinsic signal strength of the z-axis component is significantly higher than that of the x- and y- axis components (typically by one to two orders of magnitude). When noise of the same magnitude level is suppressed, the relative improvement in the corrected signal is less pronounced than that observed in the horizontal components.

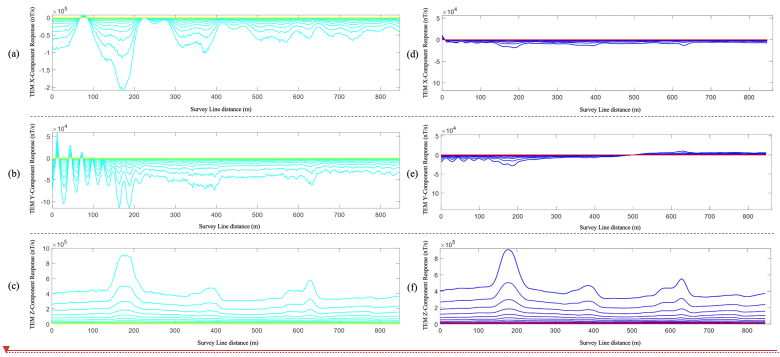

Figure 10 3-Component TEM Response. (a) TEM response of X-Component before calibration; (b) TEM response of Y-Component before calibration; (c) TEM response of Z-Component before calibration; (d) TEM response of X-Component after calibration; (e) TEM response of Y-Component after calibration; (f) TEM response of Z-Component after calibration;

5 Application

To evaluate the performance of proposed system, a TEM survey was conducted in a geologically hazardous area in Ordos, Inner Mongolia Autonomous Region. This area is a landslide zone overlying fragmented sandstone and loess. Figure 11(a) shows the planned survey line and the actual flight trajectory of this survey.

The system parameters used in this survey were:

(1) Transmission current: 20A;

(2) Transmission frequency: 25Hz;

(3) Duty cycle: 25%;

(4) Sampling rate: 1Mbps;

(5) Flight speed: 2-4 m/s;

(6) UAV platform: DJI T100;

(7) Flight time: 15-20min (based on DJI T100).

Deleted:

Deleted: 8

Deleted: 9

Deleted: .

Formatted: Font: (Default) Times New Roman, (Asian) Times New Roman

Formatted: Font: (Default) Times New Roman, (Asian) Times New Roman

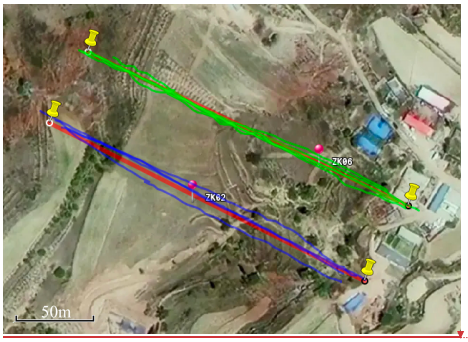



(a) (b)

Deleted:

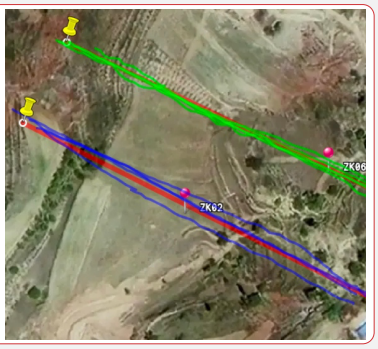

Figure 11 Proposed system in application. (a) Planned survey line and actual flight trajectory; (b) Picture of system in exploration

Deleted: 9

The inversion result of resistivity profile is shown in Fig. 12. According to the geological data, the upper layer is mainly Quaternary (Q3) loess-like silt and loess-like clay, while the lower layer primarily consists of fractured and strongly weathered Triassic (T2e) mudstone and sandstone. Water infiltration along the fractures on slip surface leads to lower resistivity at depth. The low-resistivity boundary of the slip surface is clear for the identification of landslide surface. However, to obtain an accurate stratigraphic interface, the relationship between resistivity and lithology was constructed (Ruffet et al., 1995; Jin et al., 2024; Auken et al., 2017), resulting in the predicted landslide surface boundary shown by the dashed line in Fig. 12(a) & (b). Comparison results with borehole data, which is located on the survey line, is shown in Tab. 2. The error between the landslide surface depth obtained through inversion from measured data and that from actual drilling data is approximately 1 m, which indicates a well correspondence to the actual situation.

Deleted: 10

Deleted: 0

(a)

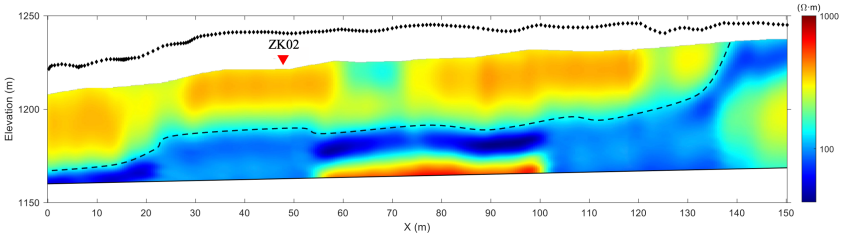

(b)

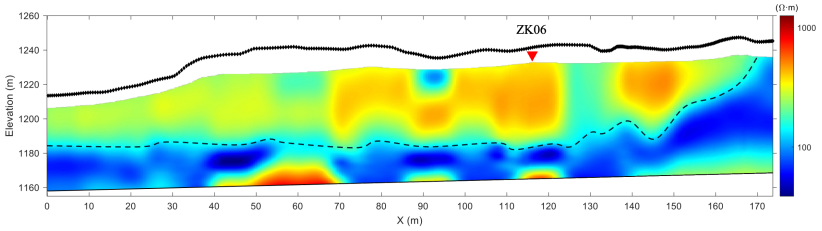

Figure 12 Inversion result as resistivity profile. (a) F6-2 resistivity profile; (b) F4-1 resistivity profile.

Table 2 Comparison of exploration result from measured data with borehole data

Observation data profile name	Borehole	Landslide Surface Depth		Error
		Drilling Data	Measured Data	
F6-2	ZK02	30.90m	31.94m	1.04m
F4-1	ZK06	47.60m	46.62m	0.98m

5 Conclusion

The successful development of the proposed system represents a breakthrough in lightweight, high-efficiency, UAV-based fully airborne TEM detection technology. Based on the field application results and interpreted data, the reliability of the proposed system has been demonstrated.

Compared with similar technologies, the existing UAV-based TEM detection mainly uses a semi-airborne configuration, which has a ground stationary transmitter and a drone-towed receiver. The proposed system developed a "air-transmitted and air-received" operation mode, representing a significant advancement in both exploration efficiency and terrain adaptability.

To achieve the above-mentioned results, the following innovations have been implemented: 1) An innovative segmented dual-clamping high-current transmission scheme was adopted to achieve narrow-pulse, high-magnetic-moment signal transmission while significantly reducing average power consumption. This fundamentally addresses the heavy payload and high power-consumption associated with traditional helicopter-borne systems. 2) A high-performance three-component electromagnetic field sensor was developed, significantly improving the sensitivity and signal-to-noise ratio of data acquisition. 3) A lightweight, transceiver-integrated towed bird was designed to improve the system's suitability for complex field application scenarios, thereby significantly enhancing exploration stability and reliability.

Despite the aforementioned advantages, UAV-based fully airborne TEM systems still suffer from transmitter turn-off dead time, which may reduce their detectability of extremely shallow targets. Furthermore, constraints on UAV payload capacity, power consumption, and flight time limit the overall system scale, thereby restricting the achievable transmitting magnetic moment and the excitation capability for deep targets. Therefore, in practical field surveys, multi-depth joint exploration

Deleted: 10

Deleted: Discussion

Deleted: marks

Deleted: the field of lightweight and high-efficiency UAV-based fully-airborne TEM detection technology

Deleted: From the application survey example and interpreted data, the proposed system is proved to be reliable. ¶

Deleted: Previous studies have demonstrated that various approaches have been developed for near-surface airborne geophysical exploration, yet each with distinct advantages and limitations. Eppelbaum and Mishne (2011) proposed the UAV-borne magnetic and VLF-EM measurements, providing a high mobility and ground-following flight capability for geophysical exploration over mountainous and complex terrain. The proposed method, however, utilized an active time-domain electromagnetic technique, can reconstruct vertical electrical structures and detect conductive targets such as water-bearing fractures even for non-magnetic subsurface media. For manned airborne electromagnetic surveys, Siemon (2012) developed precise 1-D forward and inverse algorithms for helicopter-borne high-frequency EM data, which mainly resolve shallow subsurface structures and rely on costly manned helicopter platforms with limited accessibility in rugged terrain.¶

Deleted: pioneered the

Deleted: achieving a breakthrough in both exploration efficiency and terrain adaptability.¶

Deleted: innovations are made as follows:

Deleted: An innovative segmented dual-clamping high-current transmission scheme was adopted, achieving narrow-pulse, high-magnetic-moment signal transmission while significantly reducing average power consumption.

Deleted: This fundamentally solves the problems of heavy load and high power-consumption in traditional helicopter-borne systems

Deleted: (noise level: 1.7 nT/s)

Deleted: i

Deleted: mproving the sensitivity and signal-to-noise ratio of data acquisition significantly.

Deleted: I

Deleted: ntegrated flight towed bird and compensation technology were optimized. A lightweight, transceiver-integrated towed bird was designed, making the system more suitable for complex field application scenarios, which improved the stability and reliability of exploration significantly. ¶

integrating complementary geophysical methods is required. UAV-borne magnetic surveys and ground-penetrating radar can be employed to compensate for the limitations in ultra-shallow detection.

Deleted: Apart from above mentioned advantages, UAV-based fully-airborne TEM systems still suffer from a transmitter turn-off dead-time, which may degrade the detectability of extremely shallow targets. Furthermore, the payload, power consumption and flight-time constraints of UAV platform limit the overall system scale, restricting the achievable transmitting magnetic moment and deep-signal excitation capability. In practical field surveys, multi-depth joint exploration integrating complementary geophysical methods is therefore required. UAV-borne magnetic surveys and ground-penetrating radar can be adopted to fill the gap in ultra-shallow detection, while semi-airborne TEM approaches can compensate for the insufficient deeper performance of fully UAV-borne TEM

Formatted: English (US)

6 Appendices

Code and data availability

We express our sincere gratitude for the editor's diligent attention and acknowledgment of our research endeavours. We fully acknowledge the significance of data sharing as stipulated by the journal. Figure reconstruction data of inversion results are accessible to editors and reviewers for peer review purposes undersigned confidentiality obligations (Excel datasets, DOI: https://doi.org/10.57760/sciencedb.43791). Should the esteemed editor and reviewers require further elucidation or specific inquiries pertaining to the data, we pledge our utmost commitment to providing detailed explanations and clarifications.

Team list

Author contributions

Feng Guo: Writing-original draft preparation; Resources. **Ling Huang**: Investigation; Methodology; Writing-review and editing. **Jiankai Li**: Software; Visualization. **Guangyou Fang**: Supervision. **Lihua Liu**: Project Administration. **Xiaojun Liu:** Funding acquisition

Competing interests

The authors declare that they have no conflict of interest.

Acknowledgements

Financial support

This work is sponsored by National Key R&D Program of China; **(Grant No. 2023YFC2907100)**

Deleted: National Key Research and Development Program Project "Development of Multi-parameter Airborne Electromagnetic Exploration Technology and Equipment for Mixed Field Sources

Deleted: "

Review statement

References

Auken, E., et al.: A review of airborne electromagnetic methods with focus on geotechnical and hydrological applications from the low to high moment SkyTEM system, Exploration Geophysics, 40(1), 77–87, 2009.

Auken E., Boesen T., Christiansen A. V.: A review of airborne electromagnetic methods with focus on geotechnical and hydrological applications from 2007 to 2017, Advances in geophysics, 58: 47-93, 2017.

Dadrass Javan F., Samadzadegan F., Toosi A., et al.: Unmanned aerial geophysical remote sensing: a systematic review, Remote Sensing, 17(1): 110, 2024.

Chen C. S., Chiu W. H. and Lin C. R.: Three Component Time-domain Electromagnetic surveying: Modeling and Data analysis Piers Online 4(4): 475-480, 2008.

Christiansen, A. V., Auken, E.: A global measure for depth of investigation, Geophysics, 77(4), WB171–WB177, 2012.

Eppelbaum L.V. and Mishne, A.R.: Unmanned Airborne Magnetic and VLF Investigations: Effective Geophysical Methodology of the Near Future, Positioning, 2, No. 3, 112-133, 2011.

Jin S., Sheng Y., Liu C., et al.: A review of relationship between the metallogenic system of metallic mineral deposits and lithospheric electrical structure: Insight from magnetotelluric imaging, Minerals, 14(6): 541, 2024.

Kolster, M. E., Wigh, M. D., Lima Simões da Silva, E., Bjerg Vilhelmsen, T., and Døssing, A.: High-Speed Magnetic Surveying for Unexploded Ordnance Using UAV Systems, Remote Sensing, 14, 1134, 2022.

Laizer P. L., Mulibo G. D.: Subsurface structures from geophysical data interpretation related to gold mineralisation in Sekenke-Kirondatal, SW of Iramba–Sekenke Greenstone belt, Tanzania, Model. Earth. Syst. Environ., 11(3): 226, 2025.

López Y. Á., Garcia-Fernandez M., Alvarez-Narciandi G., et al.: Unmanned aerial vehicle-based ground-penetrating radar systems: A review, IEEE Geoscience and Remote Sensing Magazine, 10(2): 66-86, 2022.

Macnae, J. C., Lamontagne, Y., West, G. F.: Noise processing techniques for time-domain EM systems, Geophysics, 49(7), 934–948, 1984.

Martelet G., Gloaguen E., Døssing A., et al.: Airborne/UAV multisensor surveys enhance the geological mapping and 3d model of a pseudo-skarn deposit in Ploumanac'h, French Brittany, Minerals, 11, 1259, 2021.

Metwally, I. A.: Design of Different Self-Integrating and Differentiating Rogowski Coils for Measuring Large-Magnitude Fast Impulse Currents, IEEE Transactions on Instrumentation and Measurement, 62(8), 2248–2257, 2013.

Nabighian, M. N.: Quasi-static transient response of a conducting half-space—An approximate representation, Geophysics, 44(10), 1700–1705, 1979.

Nabighian, M. N., Macnae, J. C.: Time-domain electromagnetic prospecting methods, in: Nabighian, M. N. (Ed.), Electromagnetic Methods in Applied Geophysics, Vol. 2, Society of Exploration Geophysicists, Tulsa, pp. 427–520, 1991.

Nicklas S. N., Kristoffer S. M.: Developing a fully airborne drone TEM system, Australian Society of Exploration Geophysicists Extended Abstracts, Volume 2023 (2), 8th International Airborne Electromagnetics Workshop, Fitzroy Island, 2023. https://doi.org/10.5281/zenodo.10060381

Noviello, C., Esposito G., Catapano I., Soldovieri F.; Multilines imaging approach for mini-UAV radar imaging system, IEEE Geosci. Remote Sens. Lett, 19, 1-5, 2021.

Nyboe N. S., Pfaffhuber A. A., Mohr K. S., et al.: Testing an airborne TEM system in Denmark using a heavy-lift drone, NSG 2024 4th Conference on Airborne, Drone and Robotic Geophysics, European Association of Geoscientists & Engineers, 2024(1): 1-5, 2024.

Pirttijärvi M., Saartenoja A., Korkeakangas P.: Drone-based electromagnetic survey system for geophysical applications, Open Research Europe, 2: 3, 2022.

Podgorski J. E., Auken E., Schamper C., et al.: Processing and inversion of commercial helicopter time-domain electromagnetic data for environmental assessments and geologic and hydrologic mapping, Geophysics, 78, E149–E159, 2013.

Raiche, A. P., Gallagher, R. G.: Apparent resistivity and diffusion velocity, Geophysics, 50(10), 1628–1633, 1985.

Ruffet C., Darot M., Gueguen Y.. Surface conductivity in rocks: a review, Surveys in geophysics, 16(1): 83-105, 1995.

Siemon, B., Steuer, A.: Airborne Geophysical Investigation of Groundwater Resources in Northern Sumatra After the Tsunami of 2004, INTECH Open Access Publisher: Rijeka, Croatia, 2011.

Siemon, B.: Accurate 1D forward and inverse modeling of high-frequency helicopter-borne electromagnetic data, Geophysics, 77, NO. 4, WB71–WB87, 2012.

Spies, B. R.: Depth of investigation in electromagnetic sounding methods, Geophysics, 54(7), 872–888, 1989.

Steuer A., Smirnova M., Becken M., et al.: Comparison of novel semi-airborne electromagnetic data with multi-scale geophysical, petrophysical and geological data from Schleiz, Germany, J. Appl. Geophys., 182, 104172, 2020.

Tang Z., Wang B., Xu Z., et al. Research on the Application of Drone Full Airborne Transient Electromagnetic Technology in Goaf Detection. arXiv [preprint], https://doi.org/10.21203/rs.3.rs-8586209/v1, 2026.

Tumański, S.: Induction coil sensors—a review, Measurement Science and Technology, 18(3), R31–R46, 2007.

Wang Y., Zhai S., Zhang X., et al.: Research on the application of UAV airborne transient electromagnetic in the detection of shallow sliding surface, IOP Conference Series: Earth and Environmental Science. IOP Publishing, 660(1): 012127, 2021.

Wu X., Xue G., Fang G., et al.: The development and applications of the semi-airborne electromagnetic system in China, IEEE Access, 7, 104956–104966, 2019.

Yu C., Xue G., Liu X., et al.: Three-component response of transient electromagnetic method, IOP Conference Series: Earth and Environmental Science. IOP Publishing, 660(1): 012055, 2021.

Page 6: [1] Deleted 丰郭 **10/22/26 2:57:00 PM**

Page 10: [2] Formatted 丰郭 **10/29/26 3:25:00 PM**

Font: 10 pt, (Asian) Chinese (China), (Other) English (US)

Page 10: [3] Formatted 丰郭 **10/29/26 3:25:00 PM**

Font: 10 pt, (Asian) Chinese (China), (Other) English (US)

Page 10: [4] Formatted 丰郭 **10/29/26 3:25:00 PM**

Font: 10 pt, (Asian) Chinese (China), (Other) English (US)

Page 10: [5] Formatted 丰郭 **10/29/26 7:59:00 PM**

Space Before: 0 pt, Line spacing: 1.5 lines, Tab stops: Not at 8 cm + 16 cm

Page 10: [6] Formatted 丰郭 **10/29/26 3:25:00 PM**

Font: 10 pt, (Asian) Chinese (China), (Other) English (US)

Page 10: [7] Formatted 丰郭 **10/29/26 3:25:00 PM**

Font: 10 pt, (Asian) Chinese (China), (Other) English (US)

Page 10: [8] Formatted 丰郭 **10/29/26 3:25:00 PM**

Font: 10 pt, Not Italic, (Asian) Chinese (China), (Other) English (US)

Page 10: [9] Formatted 丰郭 **10/29/26 3:25:00 PM**

Font: 10 pt, (Asian) Chinese (China), (Other) English (US)

Page 10: [10] Formatted 丰郭 **10/29/26 3:25:00 PM**

Font: 10 pt, Not Italic, (Asian) Chinese (China), (Other) English (US)

Page 10: [11] Formatted 丰郭 **10/29/26 3:31:00 PM**

Font: 10 pt, (Asian) Chinese (China), (Other) English (US), Superscript

Page 10: [12] Formatted 丰郭 **10/29/26 3:25:00 PM**

Font: 10 pt, (Asian) Chinese (China), (Other) English (US)

Page 10: [13] Formatted 丰郭 **10/29/26 3:25:00 PM**

Font: 10 pt, (Asian) Chinese (China), (Other) English (US)

Page 10: [14] Formatted 丰郭 **10/29/26 3:25:00 PM**

Font: 10 pt, Not Italic, (Asian) Chinese (China), (Other) English (US)

Page 10: [15] Formatted 丰郭 **10/29/26 3:25:00 PM**

Font: 10 pt, (Asian) Chinese (China), (Other) English (US)

Page 10: [16] Formatted 丰郭 **10/29/26 3:25:00 PM**

Font: 10 pt, (Asian) Chinese (China), (Other) English (US)

Page 10: [17] Formatted 丰郭 **10/29/26 4:47:00 PM**

Space Before: 0 pt, Line spacing: 1.5 lines, Tab stops: Not at 8 cm + 16 cm

Page 10: [18] Formatted 丰郭 **10/29/26 3:25:00 PM**

Font: 10 pt, (Asian) Chinese (China), (Other) English (US)

Page 10: [19] Formatted 丰郭 **10/29/26 3:25:00 PM**

Font: 10 pt, (Asian) Chinese (China), (Other) English (US)

Page 10: [20] Formatted 丰郭 **10/29/26 3:25:00 PM**

Font: 10 pt, (Asian) Chinese (China), (Other) English (US)

Page 10: [21] Formatted 丰郭 **10/29/26 3:25:00 PM**

Font: 10 pt, (Asian) Chinese (China), (Other) English (US)

Page 10: [22] Formatted 丰郭 **10/29/26 3:25:00 PM**

Font: 10 pt, (Asian) Chinese (China), (Other) English (US)

Page 10: [23] Formatted 丰郭 **10/29/26 3:25:00 PM**

Font: 10 pt, (Asian) Chinese (China), (Other) English (US)

Page 10: [24] Formatted 丰郭 **10/29/26 3:25:00 PM**

Font: 10 pt, (Asian) Chinese (China), (Other) English (US)

Page 10: [25] Formatted 丰郭 **10/29/26 3:25:00 PM**

Font: 10 pt, (Asian) Chinese (China), (Other) English (US)

Page 10: [26] Formatted 丰郭 **10/29/26 3:25:00 PM**

Font: 10 pt, (Asian) Chinese (China), (Other) English (US)

Page 10: [27] Formatted 丰郭 **10/29/26 3:25:00 PM**

Font: 10 pt, (Asian) Chinese (China), (Other) English (US)

Page 10: [28] Formatted 丰郭 **10/29/26 3:25:00 PM**

Font: 10 pt, (Asian) Chinese (China), (Other) English (US)

Page 10: [29] Formatted 丰郭 **10/29/26 3:25:00 PM**

Font: 10 pt, (Asian) Chinese (China), (Other) English (US)